



Assessment of CFD Modeling via Flow Visualization in Cold Spray Process

B. Samareh, O. Stier, V. Lüthen, and A. Dolatabadi

(Submitted May 22, 2009; in revised form June 23, 2009)

The two-phase flow properties of copper particle laden nitrogen are computationally modeled and compared with the data obtained from the experiments, determining the achievable degree of consistency between model and reality. Two common, commercial nozzles are studied. A two-way coupled Lagrangian scheme along with the RSM turbulence model is used to track the particles and to model the interactions between the gas and the particulate phase. Significant agreement is found for the geometrical gas flow structure, the resulting particle velocities, and the dependence of the two-phase flow on the particulate phase mass loading. The particle velocities decrease with increasing mass loading, even for modest powder feed rates of <3 g/s. The velocity drop occurs even when the gas flow rate is kept constant. Adiabatic gas flow models neglecting the energy consumption by the particles are thus inaccurate, except for very dilute suspensions with low technical relevance. For the cases modeled, the experiments evidence the high predictive power of the chosen CFD approach.

Keywords cold spray process, flow visualization, fluid dynamics, numerical modeling, particle dynamics, particle-shock interactions

1. Introduction

Along with the rapid experimental and technological progress in cold spray (Ref 1, 2), theoretical modeling of the particle acceleration has supported and guided the development of nearly all spray equipments available today, including HVOF and plasma torches. The gas dynamics of two-phase flows in De Laval nozzles (Ref 3), as developed around the fifties of the last century for the construction of rocket propulsion engines, was readily adopted to design nozzles for giving thrust to all kinds of powder materials suited for coating buildup. The method of characteristics has even lent its name to well-known nozzles commercialized by the leading vendor of industrial strength high-pressure cold spray equipments. During the past decade, computational fluid dynamics (CFD) made increasingly important contributions to the design of thermal spray nozzles (Ref 4, 5) (published in German). The bow shock in front of substrates (Ref 6), particle penetration to the bow shock (Ref 4), the effect of stand-off distance and angle (Ref 7, 8), and other topics have been analyzed in theory based on CFD. In addition, few studies addressed the effect of particle loading on particle

velocity or deposition rate (Ref 9–12). It was found that some predictions depend on the chosen scheme, or even software package, which particularly applies to the turbulence, drag, and heat transfer models. To establish a safer computational basis, systematic comparisons between calculations and measurements were made by several authors (Ref 4, 13). In this paper, we put new emphasis on the accuracy of CFD based two-phase flow modeling, taking advantage of a high quality flow imaging system operated in connection with particle image velocimetry. With that setup, consistent measurements of the particles and the propellant flows have been recorded which provide a unique data source for a quantitative assessment of CFD models.

Nomenclature	
A	cross-sectional area of the particle, m^2
C_D	drag coefficient
D	particle diameter, m
F_b	body force, N
Ma	Mach number
m	mass, kg
R	specific gas constant, J/kg K
Re	Reynolds number
T	temperature, K
t	time, s
V	velocity vector, m/s
ρ	density, kg/m^3
γ	specific heat ratio
μ	molecular viscosity, kg/m s

Subscripts	
p	particles
g	gas

B. Samareh and **A. Dolatabadi**, Department of Mechanical & Industrial Engineering, Concordia University, Montreal, QC, Canada; and **O. Stier** and **V. Lüthen**, Siemens AG, Corporate Technology, CT MM 5, Siemensdamm 50, 13629 Berlin, Germany. Contact e-mails: dolat@me.concordia.ca and dolat@encs.concordia.ca.



2. Methodology

2.1 Geometry

A schematic of the cold spray nozzles used in this study is shown in Fig. 1. Both nozzles have a circular cross section. Exit to throat area ratio is 9.6 and 5.9 for nozzle 1 and 2, respectively. The length of the diverging section for nozzle 1 and 2 are 69.9 and 130.3 mm, respectively. A stagnation chamber with a diameter of 14 mm is attached to the beginning of each nozzle in order to stabilize the flow and to accommodate the injection port assembly. The particle feeder, having a diameter of 3 mm, is located 50 mm upstream of the nozzle throat, and injects the copper powder axially.

2.2 Computational Domain

The computational domain is partitioned into a number of quadrilateral cells with all the variables and fluid properties stored at the nodes. For both nozzles, the total number of axial and radial cells inside the assembly of the stagnation chamber and the nozzle are 1350 and 100, respectively. Outside the nozzles, there are 1400 axial and 300 radial cells. A grid dependency study was also performed to ensure that the solution dependency on the grid size to be $<2\%$. The orientation of the nozzle and the particle feeder will allow having an axis of symmetry. As a result, a two-dimensional axisymmetric model is adequate, and will result in a considerable reduction in the computational time. FLUENT version 6.3 is used as the CFD solver in this study.

2.3 Boundary Conditions

In order to model the effect of particle loading on the strength and location of the shock diamonds, two different approaches are benchmarked. In the first approach, using nozzle 1, the mass flow rate is kept constant while loading is increased from 0 to 12%. In order to achieve this goal, the inlet pressure is increased accordingly to compensate for the energy loss due to the powder injection. In the second approach, three different loading scenarios of 0, 4, and 12% are devised for nozzle 2. As in the experiments, the inlet stagnation pressure is set to be 30 bar (absolute) and the inlet temperature is set to be 614 K, which produces a mass flow rate of 27.5 g/s as observed in the experiment without powder injection. The velocity inside the stagnation chamber is negligible and therefore, the total and static pressure and temperature are equal.

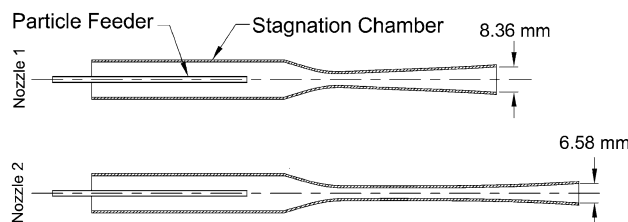


Fig. 1 Schematic of the nozzle geometry

In both cases, at the nozzle inlet, the turbulence intensity is 1% and the length scale is set to be 20% of the throat diameter, as previously proposed in Ref 7. On all surrounding boundaries, since they are far enough to have no effect on the flow field, pressure is set to the atmospheric pressure measured during the experiment.

In addition to the free jet simulations discussed above, nozzle 2 is used to model and study the effect of substrate on the flow field. In this case, a substrate is located at a distance of 30 mm from the nozzle exit. Experimental results for no loading condition are available and are compared to the simulated counterparts. Additionally, three different loading scenarios of 4, 12, and 20% are numerically modeled to study the effect of loading on the impact velocity of particles on the substrate.

The particle size distribution used in the simulations is equivalent to the distribution shown in Fig. 2. A MATLAB (The MathWorks Inc.) code was developed to generate the authentic distribution to be used in the simulations. In order to obtain reliable statistical data and to resemble the stochastic behavior of the particles inside the flow field, at each injection time step, particles are injected at random initial positions inside the projected area of the powder feeder. Particles velocity and temperature at the injection point are set to be equal to the corresponding gas phase values to resemble the experiments.

2.4 Gas Phase

In order to have the compressibility effects taken into account, the ideal gas law is used to calculate the density. The compressibility factor for nitrogen exhibits $<4\%$ deviation from the ideal gas value for pressures and temperatures up to 10 MPa and 900 K, respectively, which justifies the assumption of ideal gas behavior. Since the flow is highly compressible, viscosity changes with temperature become important. Therefore, a three coefficient Sutherland viscosity law is utilized, which is specially suggested for high speed compressible gas flows (Ref 14). A coupled implicit pressure-based solver along with the Green-Gauss node based gradient method is used to simulate the gas phase. The pressure term has second-order accuracy, while the momentum and density terms are modeled using the QUICK discretization scheme. For highly compressible flows with shocks, the first-order upwind scheme tends to smooth the shocks; hence, application of the QUICK scheme for the density and momentum terms are highly favorable using quadrilateral mesh (Ref 14, 15).

Due to the presence of shock diamonds, the flow will experience sharp gradients and steep changes in pressure and velocity. In order to accurately capture the turbulent flow features, the Reynolds Stress Model (RSM) is used as it takes into account the compressibility effects as well as the streamline curvature, swirl, rotation, and rapid changes in strain rate in a more rigorous manner compared to the $k-\epsilon$ model, and will result in higher precision (Ref 16, 17). However, as this method creates a high degree of coupling between the momentum equation and the turbulence stresses in the flow, calculations can be more susceptible to stability and convergence difficulties

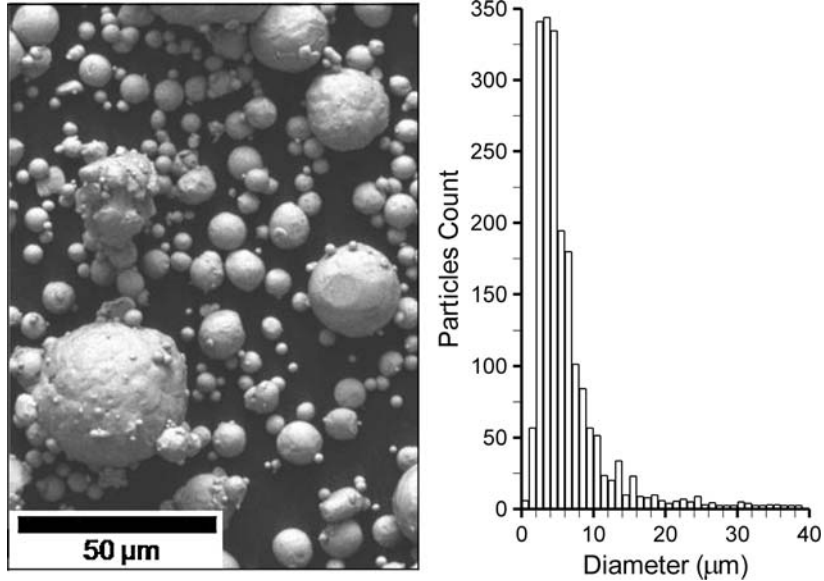


Fig. 2 Copper powder used in the experiments

compared to the k - ε model. In order to overcome this problem, for each case, the calculation begins with the k - ε model with low under-relaxation factors, and then follows with the RSM scheme.

2.5 Particulate Phase

A two-way coupled Lagrangian approach is used to obtain the particles trajectories and to model the effect of the particulate phase on the gas phase. In this method, the change in the momentum of a particle is examined as it passes through each control volume, then it appears as a momentum sink or source in the calculation of the continuous phase momentum balance. The energy exchange term is calculated in the same fashion by monitoring the change in the internal energy of the particles. Particle velocity can be obtained by integrating the force balance equation exerted on each particle.

$$m_p \frac{dV_p}{dt} = C_D \rho_g (V_g - V_p) (|V_g - V_p|) \frac{A_p}{2} + F_b \quad (\text{Eq 1})$$

Particle position at any time step can be derived by further integration of Eq 1. An additional body force term is embedded into Eq 1 which accounts for the effect of the pressure gradients caused by the shock diamonds. As particles pass through the shocks, this term will include the acceleration or deceleration of particles which arises due to the abrupt changes in the gas pressure. The body force per unit particle mass can be presented as

$$F_b = (\rho / \rho_p) V_p \nabla V_g \quad (\text{Eq 2})$$

One of the important factors which has a significant impact on the accuracy of the particle velocity and trajectory prediction is the drag coefficient. In highly compressible flows, C_D is a strong function of the particle Reynolds and Mach number based on the relative velocity of the gas and particle, Re_p and Ma_p , respectively, which are defined as

$$Re_p = \frac{\rho_g |V_g - V_p| D}{\mu_g} \quad (\text{Eq 3})$$

$$Ma_p = \frac{|V_g - V_p|}{\sqrt{\gamma R T_g}} \quad (\text{Eq 4})$$

The drag coefficient is modeled using a correlation proposed by Crowe (Ref 18) which covers a large range of particle Mach and Reynolds numbers ($0.1 < Ma_p < 2$ and $0.2 < Re_p < 10^4$). This range is sufficient for a typical cold spray process and will accommodate all the conditions encountered within the flow field except for a small region near the particle feeder where the gas and particles velocities are identical. Particles behavior in this region will not affect the flow field development, and no potential inaccuracy will be introduced. The equation proposed by Crowe is

$$C_D = (C_{Di} - 2) e^{-3.07 \gamma^{1/2} \left(\frac{Ma_p}{Re_p} \right)} g(Re_p) + \frac{h(Ma_p) e^{-Re_p}}{\gamma^{1/2} Ma_p} + 2 \quad (\text{Eq 5})$$

where C_{Di} is the drag coefficient of a sphere in incompressible flow, and $g(Re_p)$ and $h(Ma_p)$ are the devised functional relations defined as

$$\log_{10} g(Re_p) = 1.25 [1 + \tanh(0.77 \log_{10} Re_p - 1.92)] \quad (\text{Eq 6})$$

$$h(Ma_p) = \left[2.3 + 1.7 \left(\frac{T_p}{T_g} \right)^{1/2} \right] - 2.3 \tanh(1.17 \log_{10} Ma_p) \quad (\text{Eq 7})$$

The incompressible drag coefficient is taken from a correlation proposed by Clift et al. (Ref 19).

2.6 Experimental Technique

The measurements were carried out at Siemens Corporate Technology in Berlin on a “Kinetiks 4000/47” cold spray system (CGT GmbH, Ampfing, Germany) using the two most common CGT nozzles: A “v27” nozzle, called as 1 in the following, and a “v24” nozzle, to be called 2. The stagnation temperature of the process gas (i.e., nitrogen) is fixed at 723 K by the in-line control, prior to powder injection. Due to the admixing of ~5% powder feed carrier gas having room temperature, and due to heat losses through the stagnation chamber wall, the effective stagnation temperature at choking is 614 K. Nozzle 1 is operating at a constant gas flow rate of 25.4 g/s, while nozzle 2 is running at 30 bar absolute stagnation pressure. Copper powder, having the size distribution shown in Fig. 2, is injected into the nitrogen. Particle velocities were measured 16 mm downstream of the nozzle exit, within 2 mm radial distance from the nozzle centerline.

To create consistent data of the gas flow and the particle velocities, the latter were measured using the SprayWatch® system (Oseir Ltd., Tampere, Finland), while the gas flow was simultaneously mapped using a noncommercial optical flow imaging system developed at Siemens. Although particle velocities can be determined with 1% precision and 3% absolute accuracy, particle size information obtained from the stroboscope images is partly disguised by the optical resolution limit and the signal-to-noise ratio of the triple-exposure images. Particles smaller than 10 μm in diameter are not detected so that the smallest particles, constituting 20% of the powder mass, will artificially be missing in the measurement data. These particles are, nevertheless, fully taken into account in the numerical simulation so that their effect on the momentum and energy exchanges is appropriately included. The visible particles (larger than 10 μm) simply serve as tracers in the velocimetry of the system which is partially influenced by invisible solid mass.

To determine the particle sizes and velocities for a given flow configuration, a sequence of 50 triple-exposure images was recorded by SprayWatch® using 1 μs pulse separation and 0.1 μs pulse duration. Triplets of nominally identical looking particle shadows are extracted from each image by digital filtering. A stacked image of single particle shadows (not triplets) as extracted from a 50 images sequence is shown in Fig. 3. The shadows are blurred due to the particle motion during the illumination pulse length of 0.1 μs and, secondarily, due to imperfect collimation of the imaging optics. The largest shadow in this set stems from a particle couple, the single parts of which are optically resolved by the gray scale. When determined from such images, the diameters of particles are uncertain to $\pm 7 \mu\text{m}$. Each particle detected in an image sequence is represented by a pair of diameter and velocity values. Depending on the injection conditions, identical particles may travel through the flow along rather different trajectories, attaining different velocities at the nozzle exit. Hence, even the velocities of particles having very similar size and shape scatter significantly in a stochastic manner, with an unknown probability distribution function.

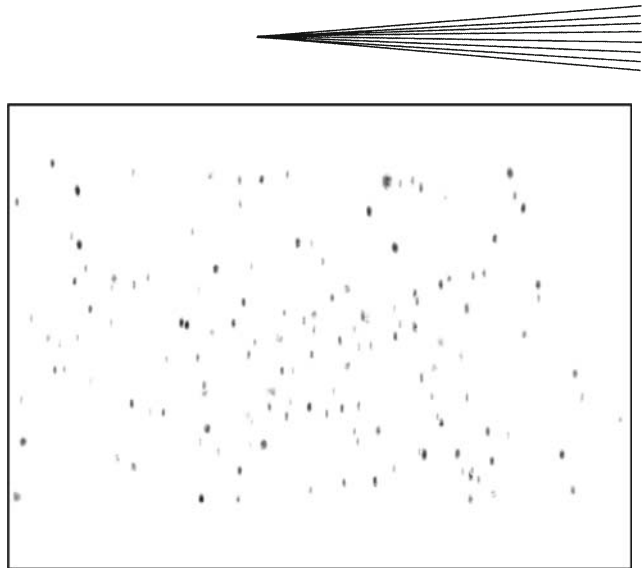


Fig. 3 Stacked image of 145 single particle shadows (not triplets) as extracted from a SprayWatch® image sequence. The particle flight direction is vertical, as seen from the longitudinal shape of most shadows. The largest shadow belongs to two optically resolved particles flying behind each other in extremely close distance. The view area is 4.0 mm wide and 3.0 mm tall

Moreover, the velocity distribution function is explicitly dependent on the particle size, but in an unknown way. Finally, the trajectory related velocity scatter is much larger than the slight influence of the powder loading fraction on the average velocity, as can be seen from Fig. 7. The small spots represent the individual particles measured at 3 g/s powder injection and exhibit a velocity scatter of 100 m/s at a given diameter. Nevertheless, it is possible to observe the loading effect and to perform a statistically significant comparison to the simulated particle velocities. To do so, the individual spots are divided by their diameters into classes containing at least 30 data points. All spots in a class have similar diameters, so that their individual velocities may be assumed to obey the same probability distribution (which may change from class to class), thus satisfying the Lindeberg condition of the central limit theorem. By the latter, the velocity mean within a class is asymptotically normal distributed, and the class size of ≥ 30 ensures that the asymptotic behavior is sufficiently approached. Thus, the class centroids may serve as auxiliary data points with normal distributed uncertainties, and their error bars are easily calculated as the chosen confidence intervals ($\pm 2\sigma$) for the average velocities. These auxiliary data points are shown in Fig. 7 together with their error bars. From them, any desired trend curve may be calculated by a parameterized maximum-likelihood method, i.e., a least-squares fit weighted by the error bars. Straight fits of this kind are also displayed in Fig. 7 and serve as guide to the eye. Based on the class centroids, the difference between 1 and 3 g/s powder feed rate is well seen to be significant, and so is the agreement with the simulated velocity mean curves also shown in Fig. 7.

As can be seen in the particle trajectories, the divergence of the particle beam is small enough to allow all

particles to pass through this detection volume, so that the observation of particles larger than $10\text{ }\mu\text{m}$ is complete. The powder injection rate is varied between 0 and 3 g/s to create various dilute suspensions. The effect of particle loading on the gas flow is clearly demonstrated even at such low feed rates, although most previous works focused on dense suspensions (Ref 20).

3. Results

When particles are injected into the gas jet, they withdraw some energy from the gas to gain kinetic energy and heat. If the injection occurs upstream of the nozzle throat, as in most cold spray systems, the nonadiabatic interaction results in a decreasing gas mass flow. A way to understand this phenomenon is to consider a constant-lag flow through the nozzle throat (Ref 3). According to this model, the transonic two-phase flow behaves very similar to the one-phase flow of a hypothetical gas with a slightly decreased specific heat ratio, γ , i.e., with more internal degrees of freedom. Under our experimental conditions, the effective γ at choking can decrease down to 1.33 from the original value for nitrogen (1.39), which causes a gas through-put reduction in the order of 2%. Thus, powder injection at constant stagnation pressure results in a decreasing gas mass flow and, hence, energy flow (power), a situation examined below using nozzle 2.

Injecting the particles to the gas flow is accompanied with a momentum exchange between the gas and solid particle phases. Particles are accelerated and the gas flow decelerates accordingly. The higher the particle loading, the larger the momentum deficit of the gas flow. Increasing the stagnation pressure will compensate the loss of kinetic energy of the gas phase due to the momentum exchange with the particle phase. Therefore, for a given particle mass flow rate, there is a stagnation pressure which results in the same mass flow rate as that of the single-phase flow. In other words, as long as the gas flow rate remains constant, the single-phase flow pattern, as characterized by the jet boundary and oblique shock angles, can be more or less recovered for the two-phase flow. Figure 4 demonstrates for nozzle 1 the persistence of the entire flow structure in spite of 12% mass loading with copper particles, due to the gas flow rate adjustment.

A visible difference between the two flows in Fig. 4 is that the separation from the interior nozzle wall occurs a bit earlier without the powder injection. Another invisible difference between the two flows is the gas temperature: Gas acceleration due to spontaneous expansion is reduced by momentum exchange with the particle phase, whereby a smaller fraction of the gas stagnation enthalpy is converted to kinetic energy. Thus, more heat will remain in the gas and result in a higher expansion temperature than for the one-phase flow. Since the temperature of a supersonic nozzle flow has, within a wide range, only a

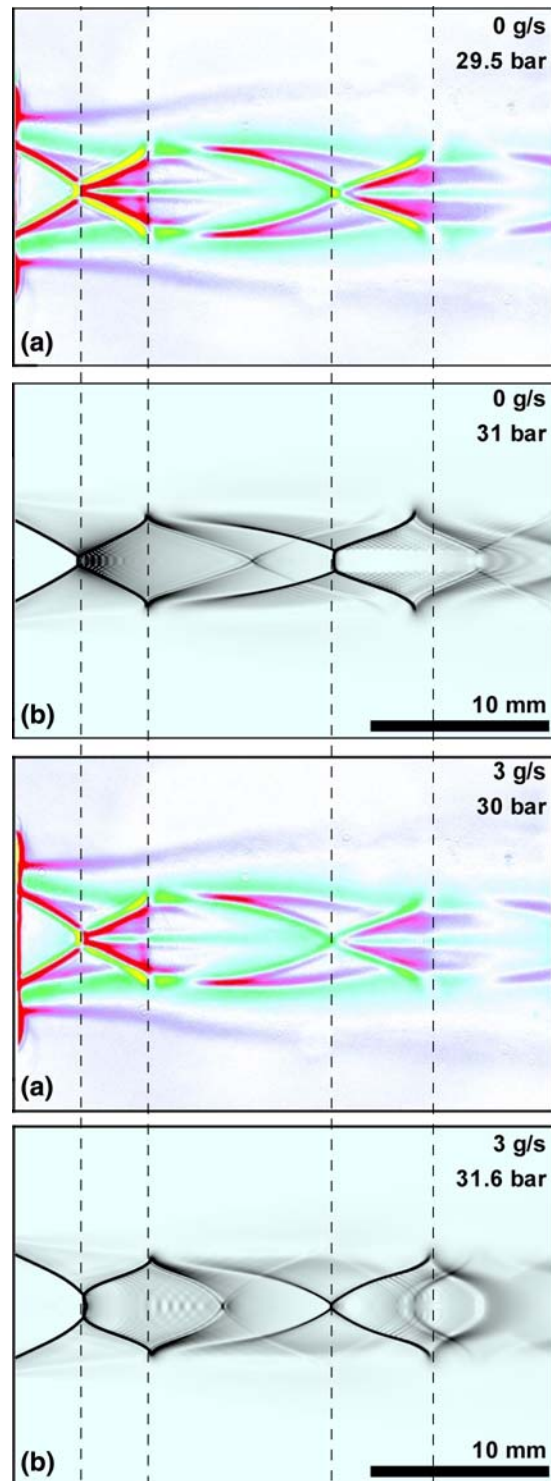


Fig. 4 (a) Measured and (b) calculated pressure gradient contours of the flow behind nozzle 1 at constant gas flow rates of 25.4 and 27.8 g/s, respectively, with and without particle injection. The uncertainties of the measured pressures and mass flow are estimated to be 1 bar and 10%, respectively. Direction is from left to right, flow separation occurs inside nozzle

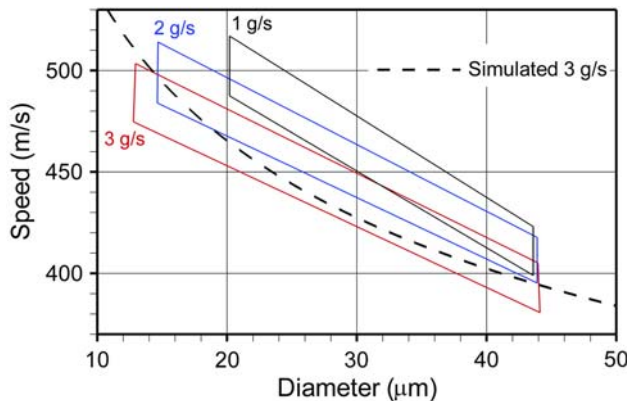


Fig. 5 Particle velocities measured in the 2-mm radial distance from the centerline of the flow behind nozzle 1, for varying injection rates. The trapezoidal regions indicate the 2σ confidence bands for the mean velocity, see Fig. 7 for further explanation

small effect on the geometrical flow pattern, the two flows in Fig. 4 look very similar.

The decreasing gas velocity at increasing feed rate is mirrored by the particle velocities, as shown in Fig. 5. Particles with 25 μm diameter lose 6% of their velocity, or 30 m/s, when the injection rate is increased from 1 g/s to 3 g/s. The calculated particles velocity for 3 g/s powder injection is also shown in this figure. As can be seen, simulated velocities are in good agreement with the experimental results.

The aforementioned case of constant stagnation pressure, but decreasing gas flow rate at increasing powder injection is analyzed using nozzle 2. The experimental flow images are shown in Fig. 6 together with numerical calculations of the respective flows. While the increasing gas temperature does not manifest itself in the geometrical flow shape, the decreasing gas flow rate leads to an observable longitudinal distortion of the flow pattern, as indicated in Fig. 6 by a shift of the dotted lines at the transition from pure gas flow to two-phase flow. All four images have the same scale and aspect ratio; so that the slightly increased Mach angles of the oblique shocks in the lower two images visualize the Mach number drop caused by momentum exchange and power loss. The flux weighted Mach number average in the nozzle exit plane decreases from 2.4 without powder to 2.1 at 3 g/s feed rate, while the gas velocity at the nozzle exit falls from 820 to 770 m/s and temperature rises by 40 K. The particle velocities reflect this trend consistently in theory and experiment, see Fig. 7. The observed deviation between measured and calculated mean velocities is <7%.

The consistency between model and measurement demonstrated by Fig. 6 shows that the calculated locations and angles of oblique shocks and jet boundaries do not differ from their measured counterparts by more than the

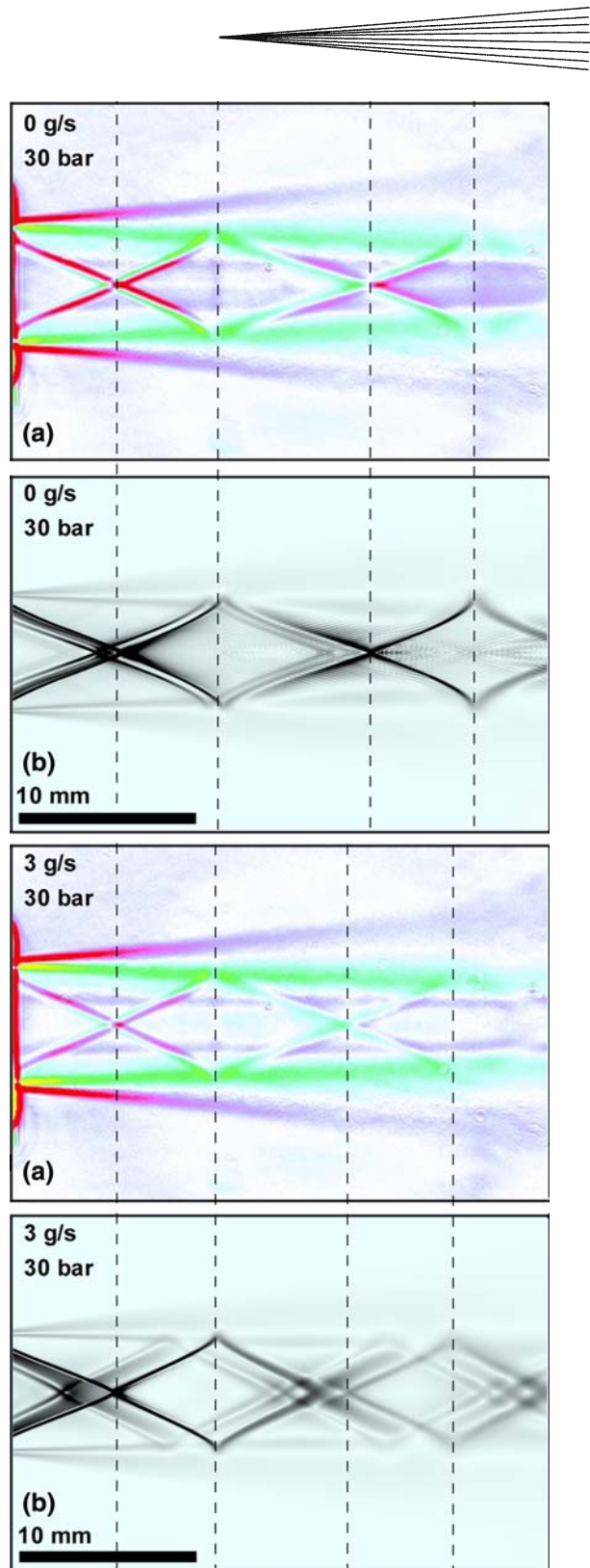


Fig. 6 (a) Measured and (b) calculated pressure gradient contours of the flow field behind nozzle 2, with particle loadings of 0 and 3 g/s, respectively, at a constant pressure of 30 bar. Gas mass flow rate drops from 27.5 to 26.4 g/s when the loading increases

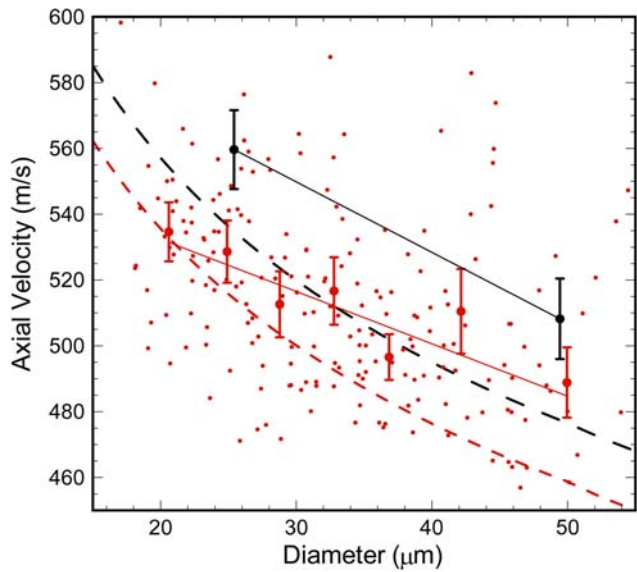


Fig. 7 Size and velocity data of single particles located at the central flow region 16 mm behind nozzle 2, at 3 g/s powder feed rate (small red spots). Associated class centroids with 2σ velocity confidence intervals (red error bar markers), and calculated size dependence of the velocity mean (red dashed line). In black: Class centroids and calculated mean velocity trend for 1 g/s powder feed rate. The thin straight lines are weighted least-squares fits to the respective class centroids. For particle diameters $\leq 40 \mu\text{m}$, the calculated and measured mean velocities differ by up to 35 m/s, or 7%

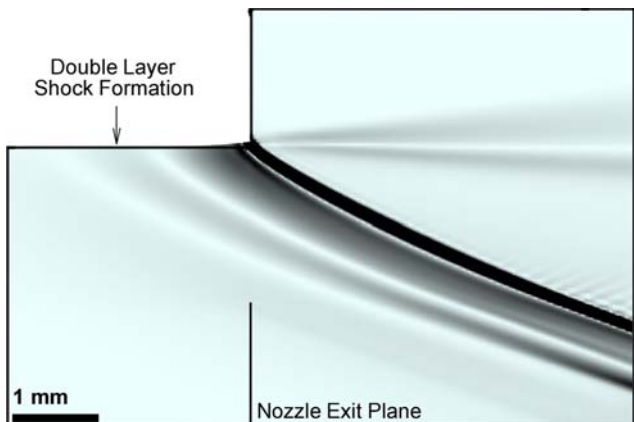


Fig. 8 Pressure gradient contour, showing where the double layer shock stems from. The wall curvature changes from convex to concave, and back to convex

uncertainty of the flow imaging. Even the observed boundary layer angle of 6° is correctly predicted by the CFD calculation. The model also seems to explain the sharpness of the tip of the first shock cone (at the leftmost dotted line in Fig. 6). While the first shock behind nozzle 1 intersects the flow axis perpendicularly (at the leftmost dotted line in Fig. 4) in accordance with classical gas dynamics, the initial Y-like shape of the first expansion wave behind nozzle 2 is unusual. According to the

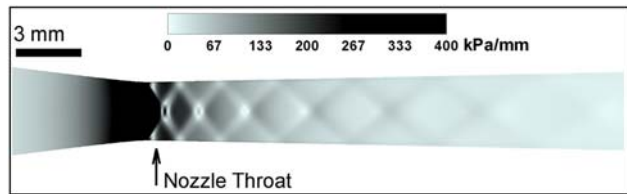


Fig. 9 Pressure gradient contours showing the shock generation at the nozzle throat and subsequent shock reflections. Nozzle 2 operating at the stagnation condition 614 K and 30 bar, without particle injection

calculations, the Y-shape results from a superposition of two expansion waves following a double layer shock. The latter is well visible from the calculated pressure gradients in Fig. 6 and originates from a tiny cavity in the nozzle contour 1.5 mm upstream of the exit. A closed-up view of that location is shown in Fig. 8. The local change of the wall curvature to negative radii causes a soft shock preceding the final shock from the nozzle exit. Such a feature does not exist in nozzle 1, as can be seen in Fig. 4. At 3 g/s powder injection, the double shock front grows in thickness and forms smoother gradients, which might possibly explain the experimental observation of decreased shock strength and a less pronounced Y shape of the expansion wave, as seen in Fig. 6.

A shock is also forming at the sharp nozzle throat, and reflected several times at the nozzle wall, as shown in Fig. 9. This causes dissipation by viscous losses and is, together with the evolution of a boundary layer, the reason why the kinetic efficiency of the nozzle does not exceed 84% at this operating condition. Due to the boundary layer growth, the maximal gas velocity is reached at 40 mm upstream of the nozzle exit. Behind this point, an almost constant gas flow provides acceleration and heating to larger particles still in lag. Figure 10 shows the calculated gas velocity profiles with and without particle injection for nozzle 2.

The effect of placement of a substrate at a standoff distance of 30 mm is studied for nozzle 2. The experimental image together with the simulated results is shown in Fig. 11. Due to the presence of the substrate, high velocity gas comes to rest in a very short distance, producing a high pressure region near the substrate. The so-called “Bow Shock” formed near the substrate has a strong effect on rendering the landing condition of small particles. Pressure gradient contours for different loadings are shown in Fig. 12. Since the flow is supersonic and is not affected by the conditions imposed downstream of the nozzle exit due to the presence of the substrate, the flow pattern must be similar to those of Fig. 6 except for the region close to the substrate where the high pressure shock is built up. Similarly, increasing the loading tends to decrease the gas flow rate and hence, results in longitudinal distortion and lower strength of shock waves. Reduced gas flow rate also manifests itself in the strength of the bow shock near the substrate. While this phenomenon is not visible in Fig. 12 due to the color scale used to

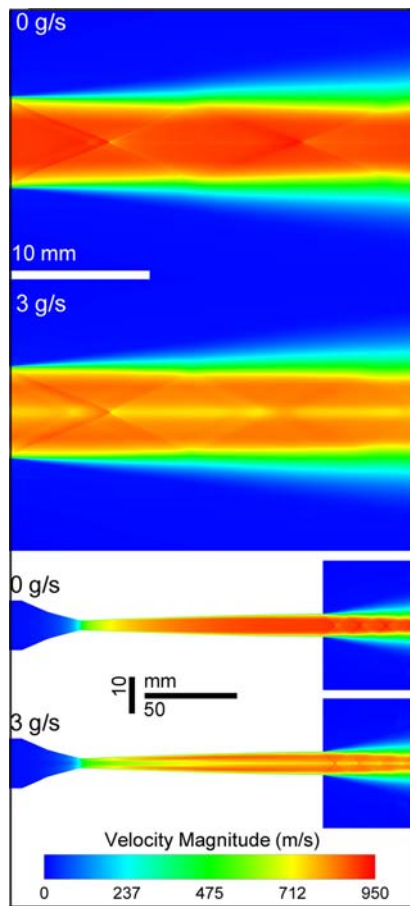


Fig. 10 Gas velocity reduction as a result of particle loading, calculated for nozzle 2 at 30 bar stagnation pressure and 614 K stagnation temperature

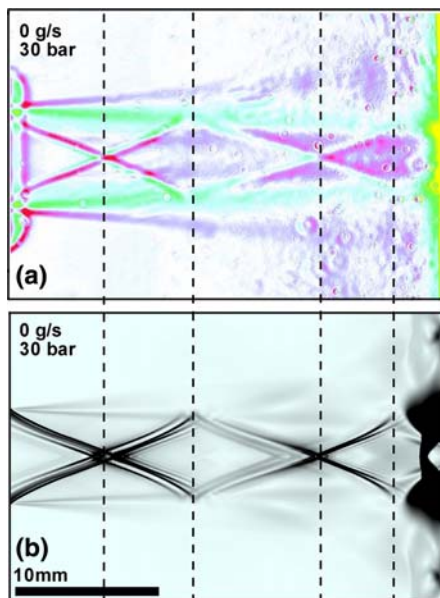


Fig. 11 (a) Measured and (b) calculated pressure gradient contours of the flow field behind nozzle 2 at a constant pressure of 30 bar, and the substrate located at 30 mm from the nozzle exit

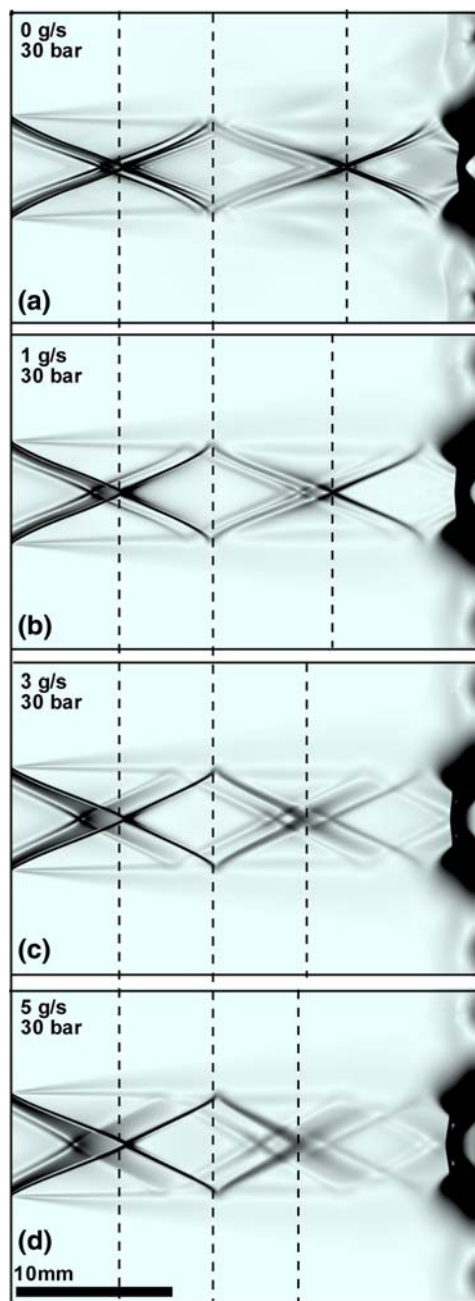


Fig. 12 Simulated pressure gradient contours for nozzle 2, operating at different loading setups of (a) 0%, (b) 4%, (c) 12%, and (d) 20%. Operating pressure is 30 bar with the substrate located at 30 mm

visualize the shock diamonds, Fig. 13, in a closed-up view of the bow shock, shows clearly that as the loading increases, the bow shock location and strength are both altered.

The effect of substrate on the impact velocity of particles is shown in Fig. 14 for three different loading cases. Free jet data are sampled from the same location as the cases with substrate, i.e., at 30 mm downstream of the nozzle exit. Comparing the velocity drop resulted from

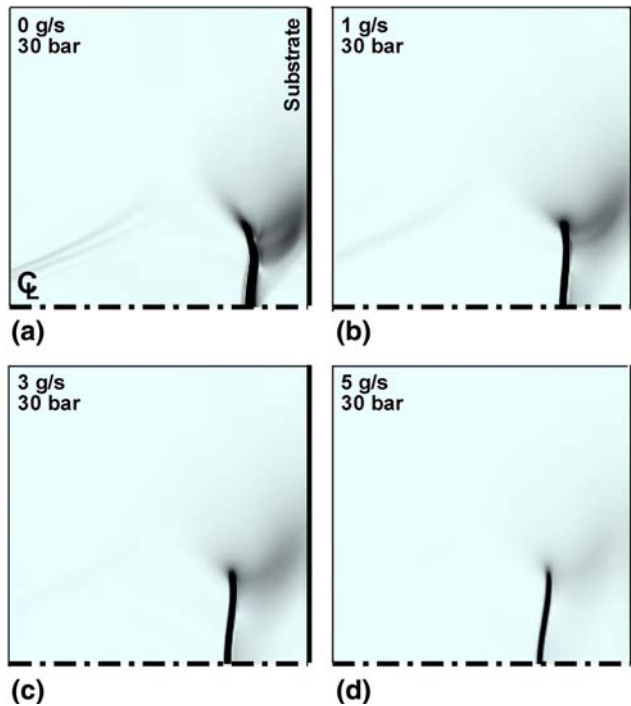


Fig. 13 Closed up view of the bow shock on the substrate for different loading cases of (a) 0%, (b) 4%, (c) 12%, and (d) 20%

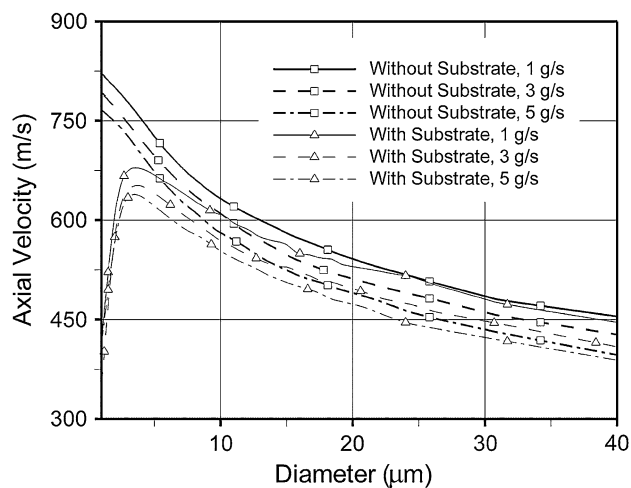


Fig. 14 Axial velocity of the particles at a distance of 30 mm from the nozzle exit, calculated for nozzle 2 at different loading conditions, with and without substrate

piercing through the bow shock to the original free jet case; the bow shock effect on small particles is quite noticeable and is even more emphasized for sizes below 5 μm . Reduction in impact velocity varies from a few meters per second for 40 μm to around 450 m/s for 2 μm particles. Such a significant effect can result in low impact velocity and dispersion of small particles, and consequently, lower deposition efficiency.

4. Conclusions

This work aims at establishing appropriate CFD schemes for modeling cold spray process by conducting a cutting-edge flow visualization and particle velocimetry experiments. It was found that using RSM, a drag law covering all speed flows, and two-way coupled Lagrangian particle tracking will result in capturing shocks and expansion waves virtually identical to those observed in the experiments. The experiments were carefully conducted and repeated to provide boundary and operating conditions for the numerical models of single-phase and two-phase flows. The effect of powder loading on the structure of supersonic two-phase flow and resultant particle velocity is presented. The powder injection rate affects the particle velocity even at modest mass loading like 10% of the gas flow. The proposed CFD model yields partially quantitative explanations for a manifold of experimentally seen phenomena of one- and two-phase flows through and behind common cold spray nozzles, including correct predictions of the velocities of spherical particles. Both numerical and experimental results clearly show that the free jet shock and expansion waves are altered when coating particles are injected at a moderate rate. For instance, the Mach number at the nozzle exit decreases from 2.4 for the free jet case to 2.1 when particles are injected at 3 g/s feed rate, while the gas velocity at the nozzle exit falls from 820 to 770 m/s and temperature rises by 40 K.

Finally, the effect of particle loading on the bow shock and consequently on the particle impact velocity were studied by placing a flat substrate at a standoff distance of 30 mm. Particles with a size of <5 μm , because of low Stokes number, have a small chance to be deposited on the substrate since they lose their kinetic energy by passing through the bow shock. By increasing the particle loading, the gas flow momentum is reduced. As a result, the stagnation pressure and the bow shock will be weakened. Therefore, moderate loadings can have dual effect on the final velocity of particles upon impact; while it reduces the gas and particle velocity in the jet, it weakens the bow shock to facilitate the deposition of particles with high Stokes numbers (i.e., larger than 15 μm in this study).

Acknowledgments

U. Pyritz, F. Heinrichsdorff, and V. Türck are gratefully acknowledged for their contributions to the measurements. A. Dolatabadi would like to thank Natural Sciences and Engineering Research Council of Canada (NSERC).

References

1. A. Papyrin, V. Kosarev, S. Klinkov, A. Alkhimov, and V. Fomin, *Cold Spray Technology*, Elsevier, Amsterdam, 2006
2. V.K. Champagne, Ed., *The Cold Spray Materials Deposition Process: Fundamentals and Applications*, Woodhead, Cambridge, UK, 2007



3. M.J. Zucrow and J.D. Hoffman, *Gas Dynamics. Volume 2: Multidimensional Flow*, Wiley, New York, 1977
4. T. Stoltenhoff, *Kaltgasspritzen von Kupfer*, Shaker Verlag, Aachen, 2004
5. A. Schwenk, Entwicklung und Erprobung neuartiger Düsen für das atmosphärische Plasma-spritzen. Werkstoffe und werkstofftechnische Anwendungen, Vol 20. TU Chemnitz, 2005
6. M. Grujicic, W.S. DeRosset, and D. Helfritch, Flow Analysis and Nozzle-Shape Optimization for the Cold-gas Dynamic-Spray Process, *J. Eng. Manuf.*, 2003, **217**, p 1603-1613
7. B. Samareh and A. Dolatabadi, A Three-Dimensional Analysis of the Cold Spray Process: The Effects of Substrate Location and Shape, *J. Therm. Spray Tech.*, 2007, **16**(16), p 634-642
8. M. Karimi, A. Fartaj, G.W. Rankin, D. Vanderzwet, J. Villafuerte, and W. Birtch, Numerical Simulation of the Cold Gas Dynamic Spray Process, *J. Therm. Spray Tech.*, 2006, **15**(4), p 518-523
9. D.L. Gilmore, R.C. Dykhuizen, R.A. Neiser, T.J. Roemer, and M.F. Smith, *J. Therm. Spray Tech.*, 1999, **8**(4), p 576-582
10. T.H. Van Steenkiste, J.R. Smith, R.E. Teets, J.J. Moleski, D.W. Gorkiewicz, R.P. Tison, D.R. Marantz, K.A. Kowalsky, W.L. Riggs, P.H. Zajchowski, B. Pilsner, R.C. McCune, and K.J. Barnett, Kinetic Spray Coatings, *Surf. Coat. Technol.*, 1999, **11**(1), p 62-71
11. K. Taylor, B. Jodoin, and J. Karov, *J. Therm. Spray Tech.*, 2006, **15**(2), p 273-279
12. W. Li and C. Li, Optimization of Spray Conditions in Cold Spraying Based on Numerical Analysis of Particle Velocity, *Trans. Nonferrous Metal. Soc. China*, 2004, **14**(Special 2), p 43-48
13. B. Jodoin, F. Raletz, and M. Vardelle, Cold Spray Flow Modeling and Validation, *Proceedings of the 2005 International Thermal Spray Conference*, 2005, Basel, Switzerland
14. Section 8.4: Viscosity, FLUENT 6.3 Documents, ANSYS Inc
15. B. Jodoin, Cold Spray Nozzle Mach Number Limitations, *J. Therm. Spray Tech.*, 2002, **11**(4), p 496-507
16. S. Sarkar, G. Erlebacher, M.Y. Hussaini, and H.O. Kreiss, Analysis and Modeling of Dilatation Term in Compressible Turbulence, *J. Fluid Mech.*, 1991, **227**, p 473-493
17. S. Sarkar and B. Lakshmanan, Application of a Reynolds Stress Turbulence Model to the Compressible Shear Layer, *AIAA J.*, 1991, **29**(5), p 743-749
18. C.T. Crowe, Drag Coefficient on Particles in a Rocket Nozzle, *AIAA J.*, 1967, **5**(5), p 1021-1022
19. R. Clift, J.R. Grace, and M.E. Weber, *Bubbles, Drops and Particles*, New York, Academic Press, 1978
20. A. Dolatabadi, J. Mostaghimi, and L. Pershin, Modeling Dense Suspension of Solid Particles in Highly Compressible Flows, *J. Comput. Fluid Dynamics*, 2004, **18**(2), p 125-131